City Research Online

City St George's, University of London

Citation: Nadimi, S. & Fonseca, J. (2018). A micro finite-element model for soil behaviour. Géotechnique, 68(4), pp. 290-302. doi: 10.1680/jgeot.16.p.147

This is the published version of the paper.

This version of the publication may differ from the final published version. To cite this item please consult the publisher's version.

Permanent repository link: https://openaccess.city.ac.uk/id/eprint/18100/

Link to published version: https://doi.org/10.1680/jgeot.16.p.147

Copyright and Reuse: Copyright and Moral Rights remain with the author(s) and/or copyright holders. Copies of full items can be used for personal research or study, educational, or not-for-profit purposes without prior permission or charge, unless otherwise indicated, provided that the authors, title and full bibliographic details are credited, a hyperlink and/or URL is given for the original metadata page and the content is not changed in any way. For full details of reuse please refer to City Research Online policy.

City Research Online: http://openaccess.city.ac.uk/ publications@citystgeorges.ac.uk

Nadimi, S. & Fonseca, J. *Géotechnique* [http://dx.doi.org/10.1680/jgeot.16.P.147]

A micro finite-element model for soil behaviour

S. NADIMI* and J. FONSECA†

This paper describes a numerical model that virtualises the fabric of a natural sand obtained from micro computed tomography (μCT) to simulate the mechanical response of the material, termed here a micro finite-element (μFE) model. The grain-to-grain interactions under loading are modelled in a framework of combined discrete–finite-element method. The basis of this approach is that using a true representation of soil fabric and deformable grains will enable a more realistic representation of the physics of granular behaviour. Each individual grain is represented in a numerical mesh and modelled as a continuum body allowed to deform according to a prescribed constitutive model with appropriate friction contact conditions. An important feature of this model is the ability to compute the map of stress distribution inside the grains. A case study of an intact sand subjected to oedometer compression is presented to demonstrate the insights that can be gained into the stress transmission mechanisms and yield initiation within the grains. The displacement field, inertia tensor and active contact number are used to quantify grain kinematics as the virtual fabric deforms. By coupling contact dynamics with contact topology, this approach provides a robust numerical tool to infer important grain scale parameters that link the micro phenomena to the macro response of soil.

KEYWORDS: fabric/structure of soils; numerical modelling; particle-scale behaviour; sands

INTRODUCTION

Since first proposed by Cundall & Strack (1979), the discrete-element method (DEM) has become a primary tool to model granular behaviour. For the most part, three-dimensional (3D) DEM models use spherical particles and, although this idealisation facilitates contact detection and force calculation, it also limits the field of application of the method (Ferellec & McDowell, 2010). As noted by Cavarretta & O'Sullivan (2012), spherical shapes cannot capture the variation in effective stiffness caused by particle rotation and inter-particle sliding observed in real sand. The effect of particle morphology on the mechanical response of granular material has been repeatedly emphasised in previous numerical and experimental studies (Oda & Iwashita, 1999; Lu & McDowell, 2007; Katagiri *et al*., 2010; Miskin & Jaeger, 2013; Nguyen *et al*., 2015). Particle shape alone can affect dilation and, consequently, the shear resistance of the material (Matsushima & Chang, 2011; Azéma & Radjai, 2012). Efforts to overcome this limitation include the use of clusters or agglomerates of spheres/discs (e.g. Lu & McDowell, 2007; Wang *et al*., 2007; Matsushima *et al*., 2009; Cil & Alshibli, 2014; Katagiri *et al*, 2014; Yang *et al*., 2016). The outcomes from these studies have highlighted the effect of overall particle shape on the rolling resistance mobilised by the multiple contact points between two particles. More advanced DEM studies using micro computed tomography (μCT) include the use of spherical harmonic-based principal component analysis (Zhou & Wang, 2017) and of non-uniform rational basis-splines and level set methods (Andrade *et al*., 2012; Kawamoto *et al*., 2016) to describe the morphological features of sand.

The rigid body conditions and associated contact laws underlying traditional DEM approaches constitute also an important limitation to accurately model granular materials, as discussed in Zheng *et al*. (2012). Conventional contact laws such as Hertz (1882) and Mindlin & Deresiewiez (1953) used for the most part in DEM studies may be of limited use for modelling contact interaction of irregular particles as demonstrated from micro-mechanical tests carried out at the grain-to-grain contact (Cavarretta *et al*., 2010; Cole *et al*., 2010; Senetakis *et al*., 2013). These studies have in particular emphasised the need to include plastic behaviour at the contacts. The DEM models used in geotechnics are still largely limited to elastic behaviour, despite the progress in developing adhesive and plastic contact laws in powder technology (Alonso-Marroquin *et al*., 2005; Luding & Bauer, 2011; Pasha *et al*., 2014; Thakur *et al*., 2014).

The diversity of grain morphologies found in natural sands leads to complex contact topologies which directly affect the stress distribution and the deformation within the granular assembly (e.g. Fonseca *et al*., 2013a; Druckrey *et al*., 2016). Contact topologies were reported to be linked to the primary fabric of stress-transmitting particles and to the realignment of the contact normal during loading (Fonseca *et al*., 2016), thus playing a key role in the mechanical response of the material. It is therefore suggested that a more accurate simulation of granular behaviour should account for particle shape, particle orientation and the associated contact topologies. This paper makes use of the numerically validated model (a micro finite-element (μFE) model) to extend it to the grain morphologies found in natural soil.

The rationale underlying this μFE model is twofold: (*a*) discrete modelling of granular systems requires a more truthful spatial distribution of the constituent grains and their morphologies, which is now possible to obtain using μCT, and (*b*) a more realistic representation of the physics of the granular behaviour can be obtained using a finite-element formulation based on deformable bodies. The model presented here makes use of the geometrical grain scale data obtained from μCT in the framework of combined discrete–finite-element method (Munjiza, 2004; Harthong *et al*., 2012) to model the individual grains and their interactions

Manuscript received 13 June 2017; revised manuscript accepted 22 June 2017.
Discussion on this paper is welcomed by the editor.
* Department of Civil Engineering, City, University of London, London, UK (Orcid:0000-0002-0971-7089).
† Department of Civil Engineering, City, University of London, London, UK (Orcid:0000-0002-7654-6005).

Offprint provided courtesy of www.icevirtuallibrary.com
Author copy for personal use, not for distribution

under loading. The idea consists of virtualising the soil fabric by meshing the constituent grains and allowing them to interact and deform according to appropriate constitutive model and frictional contact conditions. The contact response results from the deformation of contacting bodies, which accounts for the specificities of each contact surface. This discrete–finite-element method approach has the potential to elucidate the fundamental parameters that control the micro scale phenomena, thus providing a better link between the micro and macro scales. Moreover, this modelling technique can contribute insights into yield initiation within the grain, thus providing a step change for the understanding of grain breakage (to be developed in future work). The present paper focuses, first, on the methodology used to obtain the numerical fabric, including acquiring and processing the 3D images and meshing the individual grains. This is followed by a case study on one-dimensional (1D) compression of Reigate sand for which the measured micro scale data are discussed.

THE μFE MODEL

One challenge in modelling physical phenomena of real soil is obtaining a detailed numerical representation of the constituent grains to simulate grain interaction. The framework presented here makes use of advanced image processing and mesh generation techniques to obtain an accurate and computationally tractable representation of the complex geometries of real sand grains. This virtual fabric is used to compute the macroscopic global response under externally applied load and, most importantly, to investigate the micro scale phenomena that takes place. The flowchart summarising the procedure used to develop the model is presented in Fig. 1. The main stages comprise: discretising the individual grains from the tomographic data, generating the finite-element mesh and performing the numerical experiment according to the assigned constitutive behaviour. The details are provided in the three following sections on image acquisition and processing, mesh generation and a case study. The model described here follows an earlier two-dimensional (2D) version described in Nadimi *et al.* (2015). The adaptation to three dimensions is clearly challenging and required the use of more sophisticated algorithms, as described herein.

Image acquisition and processing

The internal structure of the soil is obtained from 3D images acquired using X-ray μCT. The images are maps of X-ray attenuation based on the composition of the material represented by the intensity, or colour, of each voxel (or 3D pixel). The accuracy of this 3D representation depends on the quality and detail of the images. Image quality is to a great extent controlled by the size of the focal spot and the detector pixel size, which determine the number of possible source-detector paths. The loss of definition in an image occurs when the radiation is originated over an area rather than a single point; this is called geometric unsharpness (more details can be found in Fonseca (2011)). A micro-focus tube scanner, the 'nanotom' (phoenix|x-ray, GE), is used here. This lab source has a signal-to-noise ratio comparable to synchrotron sources (Brunke *et al.*, 2008) and produces sharp images so that the boundaries of the grains can be clearly identified. The 3D images acquired have a voxel size of 5 μm, which means that each grain is represented by a large number of voxels (60 voxels across the diameter for a d_{50} of approximately 300 μm) and the overall grain shape can be well captured.

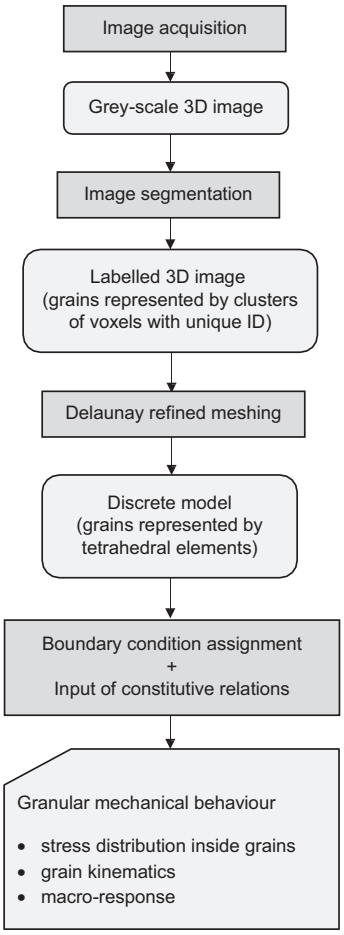

Fig. 1. Flowchart illustrating the various processes/tools and outcomes involved in the development of this μFE model

The discretisation of the individual grains consists of extracting the solid phase from the image and subsequently separating the grains touching and categorising the individual grains. This process has been documented in previous publications by the authors (Fonseca *et al.*, 2012, 2013b) and a summary is provided here for completeness. In order to identify the solid phase, a thresholding technique was employed, which consists of producing a binary image where the voxels representing the solid phase are assigned a value of 1 and the voxels representing the void phase are assigned the value of 0, based on a chosen threshold value. The threshold value was obtained by fitting a Gaussian curve to each of the two peaks of the histogram of intensity values and determining the minimum point between them. This threshold value was confirmed using Otsu's method (Otsu, 1979) employing the algorithm implemented in Image J (Schindelin *et al.*, 2015). To identify the individual grains within the solid phase a watershed approach was used. Watershed segmentation consists of taking the image as a terrain surface, where the elevations are represented by a distance map, and identifying the single grains as they were drainage basins (Beucher & Lantuejoul, 1979). The distance map was computed by calculating the number of iterations required to fill every solid region (Atwood *et al.*, 2004). The watershed algorithm employed here is based on the open-source software toolkit ITK (Ibanez *et al.*, 2005) and was applied to the inverse distance map (IDM) or height function. For each basin, it is possible to define the total depth D, which is the minimum of the height function, and a watershed depth D_e, which is the depth of water it can hold without flowing to adjacent basins. Two watershed input

Offprint provided courtesy of www.icevirtuallibrary.com
Author copy for personal use, not for distribution

parameters are used to alleviate over-segmentation, the threshold (T) and the level (l) parameters. The threshold parameter T is used to remove the small catchment basins with depth less than TD_{max}, where D_{max} is the maximum depth of all the catchment basins in the IDM. No watershed lines will be generated on the boundaries of these very small regions, and, as a result, these regions are attached to adjacent basins. The level parameter l is used to fill all the remaining basins by a flood level lD_{max}. In this way, the basins of D_e smaller than lD_{max} will be filled entirely and merged into adjacent basins. The parameters used here were $T = 0{\cdot}04$ and $l = 0{\cdot}2$. The output of the watershed segmentation is an image where each grain is defined as a set of voxels with a unique intensity value, the grain's identification (ID). This ID takes integer values between *1* and the total number of grains, whereas the voxels' ID representing the void space takes a value of *0* throughout.

Mesh generation

The meshing stage is pivotal in this work. Obtaining a mesh that is a good finite-element representation of the material is particularly challenging for complex and irregular shapes such as the ones found in real sand. The numerical mesh is therefore expected to be able to provide a good approximation of the object boundaries and, in addition, must fulfil additional constraints over shape, orientation and size of the elements.

A simple way of converting voxel data into a mesh is to use a direct conversion method that transforms each voxel or a cluster of voxels directly into a mesh. In this case, the squared elements of the mesh will result in 'stepped', non-smooth boundaries of the objects or grains. Thus, this voxelised mesh has a number of drawbacks that can affect the simulation of the object-to-object interaction. An alternative approach is to use the so-called marching cubes algorithm, first developed by Lorensen & Cline (1987), to extract a polygonal mesh from the voxel elements defining an object. This method computes a local triangulation of constant density within each voxel, resulting in a mesh of uniform resolution. The limitation of this method lies in the fact that it does not allow optimisation of the mesh size according to geometrical constraints of the object. In other words, a requirement of a good meshing approach would be to allow the use of small elements for regions of high detail and large elements, for example, on flat regions.

The surface mesh extraction technique used here is a refinement of the constrained Delaunay triangulation (Shewchuk, 2002). Delaunay refinement algorithms are powerful because they exploit several favourable characteristics of Delaunay triangulations, such as preserving boundaries and avoiding 'skinny' triangles by maximising the minimum angle of all the triangles in the triangulation. This is particularly relevant for the numerical simulation, as elements with high aspect ratio may lead to slow convergence of the finite-element solver and, therefore, avoiding these shapes is critical to reduce the processing time and consequently improve computational efficiency (see the Appendix for details). An advanced surface reconstruction algorithm is employed here that uses the open source Computational Geometry Algorithms Library (CGAL; Rineau & Yvinec, 2017).

This technique is implemented using a developed Matlab (Mathworks, 2015) script to generate the image-based mesh. The process of mesh generation comprises essentially two stages. In the first stage, triangular iso-surfaces are extracted from the 3D segmented image with pre-set values for density and the smallest angle. The density value controls the size and number of triangles representing the surface of each grain and thus, the number of nodes in the numerical analysis. The second stage consists of 'filling' the tetrahedral elements for the sub-volumes bounded by the iso-surfaces to obtain the volumetric mesh. Fig. 2 shows an example of the generated mesh. A fine mesh is used to describe more angular features of the grains (Fig. 2(a)), whereas large triangles are used in flat surfaces (Fig. 2(b)). The key advantage of the technique employed here is to preserve the original boundary of the grain with no restrictions for complex topologies.

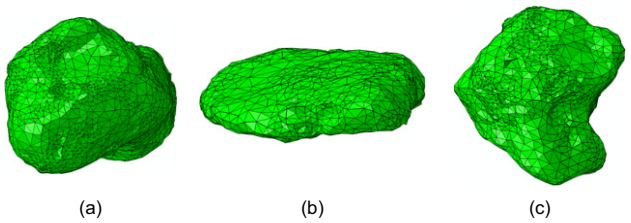

Fig. 2. Three examples of meshed grains to illustrate: (a) the finer mesh used to describe angular features of the grain; (b) the large elements used in flat regions; (c) the mesh of a concave grain

Numerical fundamentals

The numerical formulations for body deformation and body motion are presented here. In the framework of combined finite–discrete-element method, grain deformability can be described by a finite-element method formulation, whereas the motion of the individual grains and contact detection are presented using DEM principles. Deformability depends on the straining of the material rather than on its rigid body motion. If there is no strain, the grain will undergo rigid body motion only. The motion of the grains is governed by the internal forces acting on the element nodes. The nodal forces include the contribution from contact interaction, internal deformation of a discrete element and external loads

$$\mathbf{M}\frac{\partial^2 \boldsymbol{x}}{\partial t^2} + \boldsymbol{F}_{int} - \boldsymbol{F}_{ext} - \boldsymbol{F}_c = 0 \tag{1}$$

where $\boldsymbol{x}$ is the nodal displacement vector, $\boldsymbol{F}_{int}$ is the internal resisting forces vector, $\boldsymbol{F}_{ext}$ is the applied external loads vector and $\boldsymbol{F}_c$ is the contact forces vector.

The equations of motion for the body are integrated through time (t) using an explicit central difference integration rule

$$\dot{u}^{(i+1/2)} = \dot{u}^{(i-1/2)} + \frac{\Delta t^{(i+1)} + \Delta t^{(i)}}{2}\ddot{u}^{(i)} \tag{2}$$

$$u^{(i+1)} = u^{(i)} + \Delta t^{(i+1)}\dot{u}^{(i+1/2)} \tag{3}$$

where $\dot{u}$ is velocity, $\ddot{u}$ is acceleration and i refers to the increment number.

An advantage of using explicit time integration is the possibility of utilising the diagonal lumped mass matrix. Computational efficiency can be improved by using the inversion of the mass matrix, for which the computation for the accelerations at the beginning of the increment can be reduced to a simple operation (Wu, 2006)

$$\ddot{u}^{(i)} = \mathbf{M}^{-1} \cdot (\boldsymbol{F}^{(i)} - \boldsymbol{F}_I^{(i)}) \tag{4}$$

where $\mathbf{M}$ is the diagonal lumped mass matrix, $\boldsymbol{F}$ is the applied load vector and $\boldsymbol{F}_I$ is the internal force vector. The explicit procedure requires no iterations and no tangent stiffness matrix.

Offprint provided courtesy of www.icevirtuallibrary.com
Author copy for personal use, not for distribution

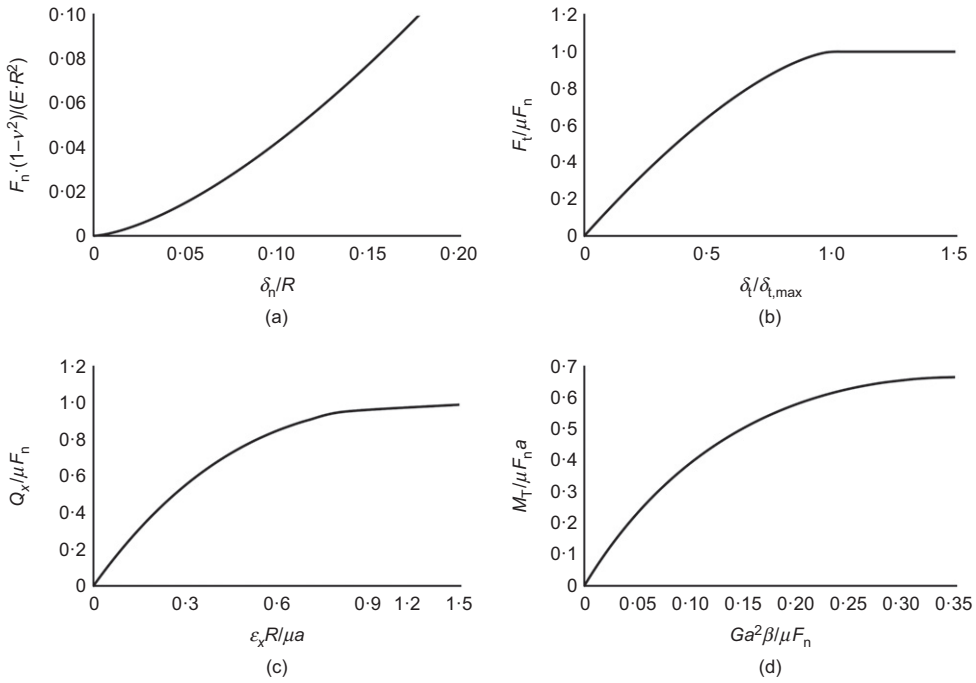

Fig. 3. Summary of contact constitutive behaviour for elastic spheres: (a) non-dimensional normal force displacement; (b) non-dimensional tangential force displacement; (c) non-dimensional rolling moment; (d) non-dimensional twisting moment

In an explicit scheme, the time step must be small enough to ensure the stability of the integration. Abaqus automatically adjusts the time increment during the analysis based on a global estimation method. The advantages of using a global time increment estimation is the constant update of the maximum frequency of the algorithm leading to a better and more stable simulation. The trial stable time increment is calculated for each element in the mesh as follows

$$\Delta t = \frac{2}{\omega_{\max}^{\text{element}}} \tag{5}$$

where $\omega_{\max}^{\text{element}}$ is the maximum eigenvalue of the element. A conservative estimation of the stable time increment is given by the minimum value taken over all elements.

The summary of the constitutive contact behaviour for an elastic sphere is provided in Fig. 3 by means of non-dimensional quantities. These solutions are reproducible in this numerical framework by considering hard contact in the normal direction and Coulomb friction in the tangential direction. The principles of using deformable spheres to simulate contact interaction for normal, tangential, rotational and torsional loading, and the numerical validation of the constitutive contact behaviour against existent theories (including mesh size dependency) will be discussed in more detail in a follow-up publication.

A CASE STUDY

A case study is presented to demonstrate the ability of the proposed μFE approach to model a sample of sand. The model runs in the Abaqus finite-element package (Dassault Systèmes, 2014) and is implemented with an explicit algorithm that uses a dynamic framework. The tetrahedral mesh generated in Matlab is first imported into the finite-element solver using a text file readable by Abaqus. The *voxel coordinates* in the Matlab matrix are converted into *object coordinates* using the resolution value of the μCT images. This section includes first a brief description of the governing equations and the numerical model. An assessment of the energy quantities is then presented, which enables: (*a*) assessment of the plausibility of the simulation to carry out quasi-static analysis and (*b*) evaluation of the assembly response in terms of plastic and frictional behaviour. This is followed by an investigation into the effect of microscopic yield stress, which will help in understanding grain breakage (to be discussed in future work). Finally, the measurement of the internal stress distribution and four-dimensional (4D) kinematics of the grains are discussed.

The model

An oedometer test on a sample of a natural sand is used. The input data consist of a high-resolution μCT image of an intact sample of Reigate sand, a quartzitic formation from southeast England, part of the Lower Greensand formation (Fonseca *et al.*, 2012). The particle size distribution is shown in Fig. 4. The sand has a median grain diameter (d_{50}) of 300 μm and is characterised by very high densities and an interlocked fabric, which enables the use of block sampling to collect intact samples (Fig. 5(a)) from an outcrop of this

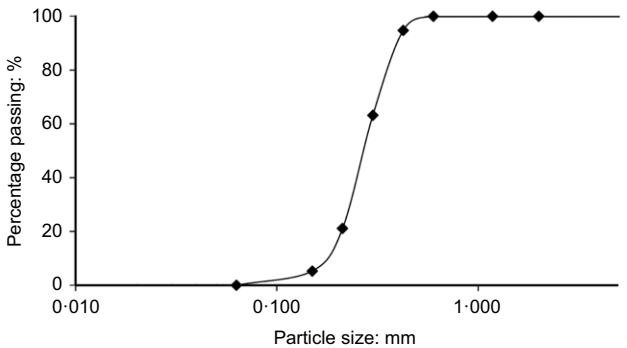

Fig. 4. Particle size distribution of Reigate sand obtained from sieving (after Fonseca *et al.*, 2012)

Offprint provided courtesy of www.icevirtuallibrary.com
Author copy for personal use, not for distribution

(a)

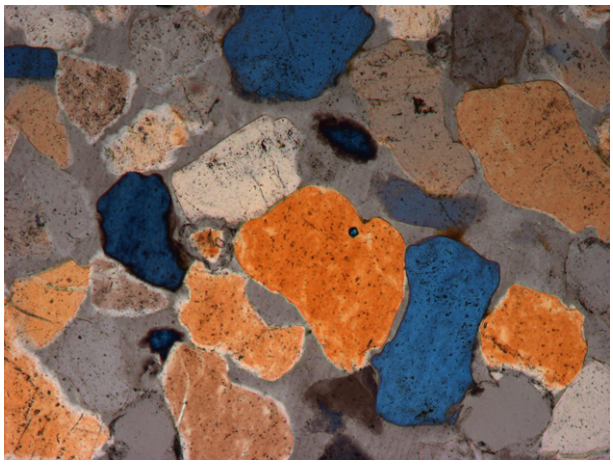

(b)

Fig. 5. Intact Reigate sand: (a) illustration of the block sample; (b) micrograph of a thin section under cross-polarised light showing the extended flat contacts between the grains (after Fonseca, 2011)

material (details in Fonseca (2011)). A minimal cement content was observed in the samples retrieved. The shapes of the grains in this geologically old, once deep, buried sand vary from near-spherical to highly non-spherical with embayments. The most striking feature of this sand is the predominance of flat, extended contacts (Fig. 5(b)), in contrast to the point contacts found in more recent sand formations or in reconstituted samples of the same sand.

The model consists, in this case, of a small sample represented by an image of $400 \times 400 \times 200$ voxels subjected to 1D compression. Fig. 6 shows a 3D view of the sample together with the boundary conditions imposed – namely, fixed lateral boundaries and displacement allowed along the vertical direction only. This is a sub-volume cropped from the larger 3D image, which explains the flat boundaries of the sample. The assembly contains 630 grains and each grain includes on average 1096 nodes and 3080 tetrahedral elements. Average values of 100 GPa for Young's modulus and 0·15 for Poisson ratio (Holtzman *et al.*, 2009) were used, corresponding to a bulk modulus of $K = 47{\cdot}6$ GPa and shear modulus of $G = 43{\cdot}5$ GPa. Plastic behaviour is assumed to initiate at 10 MPa stress using an isotropic hardening model. Subsequently, the material is allowed to harden to 110 MPa at 0·05 strain (hardening modulus, $E_t = 2$ GPa), after which it behaves as perfectly plastic. In other words, if the contact

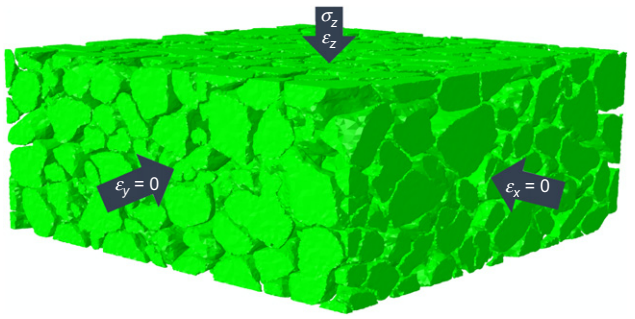

Fig. 6. Boundary conditions used for the simulation of the oedometer compression

stress decreases due to grain rearrangement, there is a residual deformation after the yield point. The yield and hardening values were obtained from curve fitting of the normal force plotted against displacement response, from single grain experiments conducted on silica sand. To account for grain breakage, a more advanced constitutive assumption is required (e.g. Nadimi & Fonseca, 2017). The coefficient of inter-particle friction for the grains was assumed to be 0·23, the value obtained from experimental grain-scale measurements on silica grains (Senetakis *et al.*, 2013). The 1D compression test was carried out under vertical displacement control, up to a vertical strain of 0·1. The analysis took 13·5 h (running on a Dell Precision T7610). For a full-size sample, such as those described in Kawamoto *et al.* (2016) and Fonseca *et al.* (2013c), the simulation is expected to take approximately 6 days.

Assessing energy quantities

When using an explicit dynamics model for a static problem, it is necessary to make sure that quasi-static conditions are maintained during the simulation. The energy balance for the model, according to the first law of thermodynamics, can be written as follows

$$E_K + E_U = \int_0^t \dot{E}_{WF} dt + \text{constant} \tag{6}$$

or

$$\int_V \frac{1}{2}\rho \boldsymbol{v} \cdot \boldsymbol{v} dV + \int_V \rho U dV = \int_0^t \dot{E}_{WF} dt + \text{constant} \tag{7}$$

where E_K is the kinetic energy, E_U is the internal energy and $\dot{E}_{WF}$ is the external work defined as the rate of work done by external forces and contact friction forces between the contact surfaces. In addition, ρ is the density, $\boldsymbol{v}$ is the velocity field vector and U is the internal energy per unit mass.

The energy quantities used here are the kinetic and internal energies. Fig. 7 shows the evolution of the kinetic and internal energies over time for the four simulations reported in this case study. It can be seen that, while the internal energy increases, the kinetic energy remains near zero throughout the whole simulation, which confirms the quasi-static nature of the process.

The effect of the yield stress

Given the difficulty in measuring microscopic yield stress and plastic behaviour of sand grains, experimental results are commonly reported in terms of force–displacement (as contact area evolves during loading). Although for the microscopic yield stress a value of 10 MPa has previously been assigned, interest also lies in investigating the effect of using different values on the macroscopic response of the assembly.

Offprint provided courtesy of www.icevirtuallibrary.com
Author copy for personal use, not for distribution

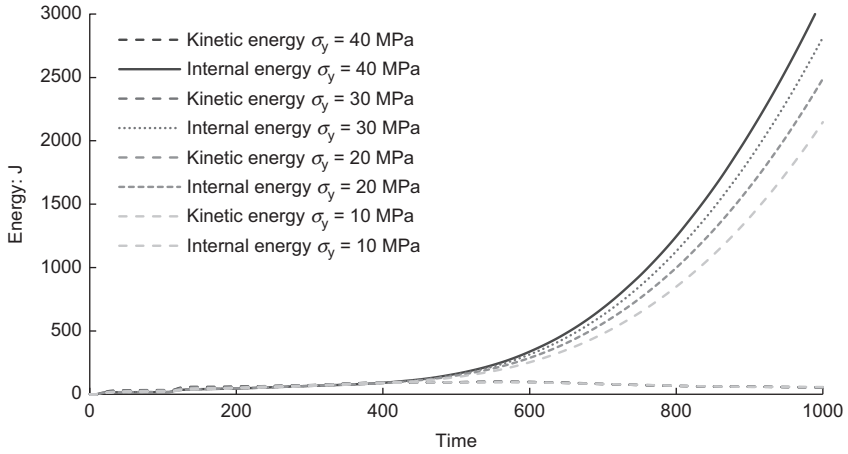

Fig. 7. Evolution of the measured kinetic and internal energies for the simulations reported in this study; the near-zero values measured for the kinetic energy demonstrate the quasi-static nature of the simulations

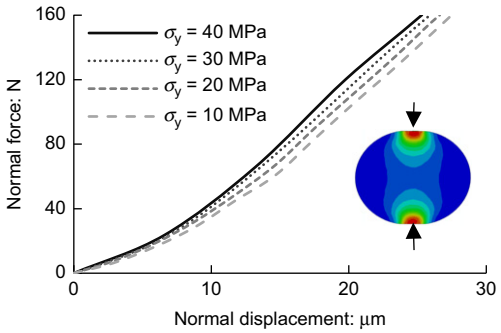

Fig. 8. Hertzian response of an elastic–plastic sphere measured for four different yield stresses and the general stress field inside the grain

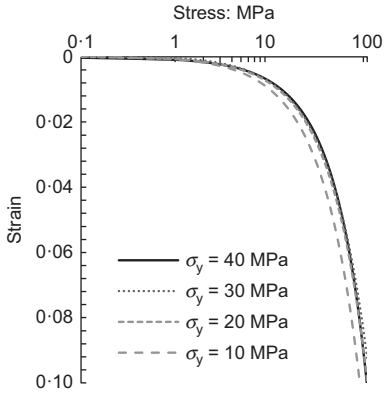

Fig. 9. Stress–strain response of the oedometer compression simulations

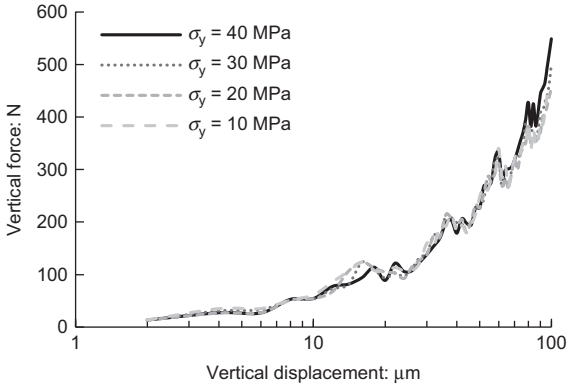

Fig. 10. Force–displacement measurements from the oedometer compression simulation

To this end, additional yield stresses of 20, 30 and 40 MPa are also used. In order to better understand the effect of yield stress and isolate it from the influence of grain shape and contact topology, the Hertzian response of elastic–plastic spherical grains was investigated with analogous constitutive behaviour, as presented in Fig. 8. This plot shows that, for a given normal force, the grains with lower yield stress exhibit larger displacement and thus softer response. The macro response of the assembly, computed based on reaction force measured at the top platen resulting from the applied displacement, is presented in terms of the stress–strain response (Fig. 9) and in terms of force–displacement (Fig. 10).

As expected, it can be seen from Fig. 10 that higher load is required for higher yield stress. This observation is in agreement with the trend presented in Fig. 7 in terms of energy quantities; that is, the internal energy is higher for higher yield stress. Traditionally used stress–strain curves cannot, however, represent this difference as shown in Fig. 9. Frictional and plastic energy dissipation for the different yield stress is reported in Figs 11 and 12, respectively. It can be observed that the plastic dissipation (Fig. 12) is one order of magnitude higher when compared to frictional dissipation (Fig. 11). This observation is believed to be related to the micro scale mechanisms that take place during 1D compression and does not apply, for example, to triaxial compression.

Grain kinematics and stress distribution inside grains

The micro scale response is investigated in terms of grain kinematics and the mechanisms of stress transmission. In order to infer grain kinematics it is necessary to compute the internal displacement field of each individual grain. The displacement or rearrangement of the grains includes a combination of rotation and translation. The displacement field is obtained from the spatial coordinates of the nodes composing each grain at subsequent time steps during deformation. Similarly, the stress distribution inside the grains is obtained from the stress values measured at each node.

Figure 13 shows a 3D view of the stress distribution in the whole assembly at three stages of loading, initial ($t = 0$), intermediate ($t = 500$) and final ($t = 1000$) using the von Mises criterion. It can be seen that, at the initial stage

Offprint provided courtesy of www.icevirtuallibrary.com
Author copy for personal use, not for distribution

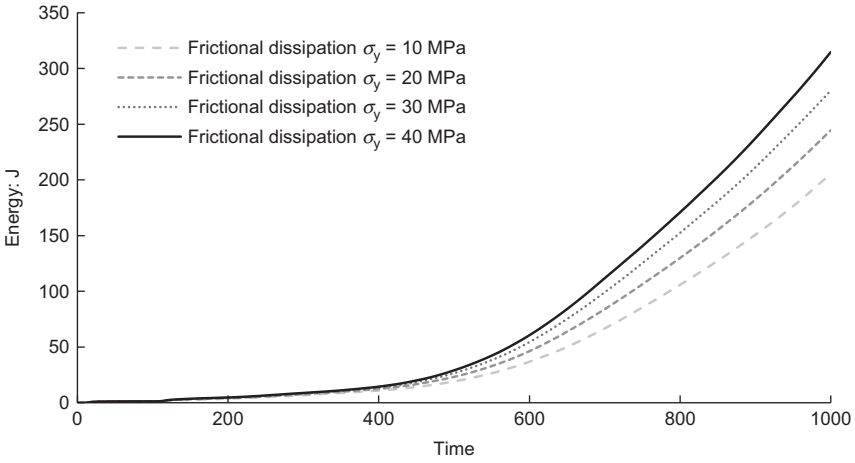

Fig. 11. Frictional dissipation measured for the four oedometer test with different yield stresses

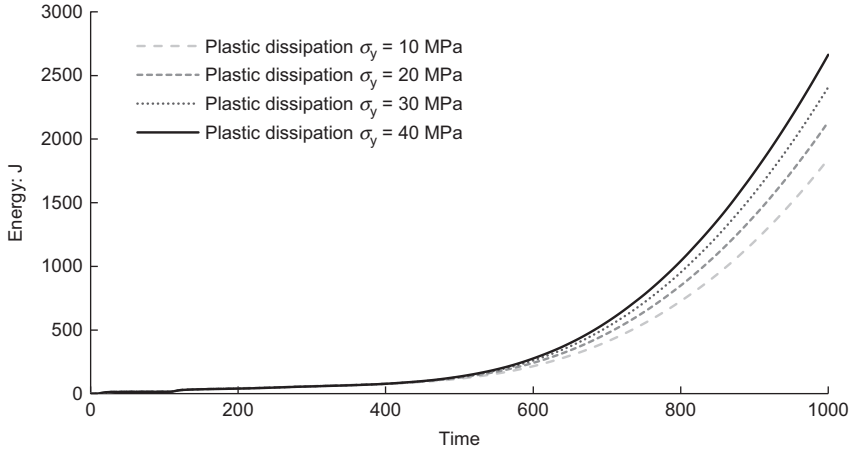

Fig. 12. Plastic dissipation measured for the four oedometer test with different yield stresses

(Fig. 13(a)), the sample is not loaded yet and all grains have a stress field constant and equal to zero. At the intermediate stage (Fig. 13(b)), it can be seen that the stress concentration starts at the grain contacts and propagates through the grain before being transmitted to another neighbouring grain, again by way of their contacts. At the final stage (Fig. 13(c)), the assembly has been heavily loaded and this is translated in the large internal stress values exhibited by the grains. These data enable the identification of the stress-transmitting particles and the investigation of the micro-mechanisms that lead to the formation of the heterogeneous networks of force transfer, the so-called 'force chains'. It is interesting to note that, despite the high levels of stress measured at the individual grains at the final loading stage, there are, however, grains that remain essentially with near-zero stress. The presence of these apparently unstressed grains surrounded by highly stressed grains is a clear indication of the heterogeneity of the contact force network that forms in stressed granular media (e.g. Radjai, 2008; Fonseca *et al.*, 2016). When using this stress distribution it is important to note that the Von Mises yield criterion is independent of the first stress invariant, while the failure condition for soil grains depends on both the first and second invariant of stress.

Figure 14 shows detailed views of the contact areas, the internal stress distribution and displacement field for single grains selected from the assembly, measured at $t = 1000$. Four grains are displayed, termed 'grain 1', 'grain 2', 'grain 3' and 'grain 4'. The contact area was obtained by computing the contact pressure at the surface of each grain (Figs 14(a), 14(d), 14(g) and 14(j)), termed here active contacts. The condition for a node to be part of an active contact is to have a contact pressure greater that zero. While these contact areas are associated with higher stress values, a stress value greater than zero is not necessarily a contact because of the stress propagation within the grain, this can be seen in Figs 14(b), 14(e), 14(h) and 14(k)). It can be observed that for 'grain 1' a constant displacement value is exhibited at all points of the grain (displacement map described by a unique shade in Fig. 14(c)) which indicates that this grain undergoes pure translational motion. In contrast, 'grain 2', 'grain 3' and 'grain 4' exhibit both translational motion and rotation. This is represented by a gradient in the shades representing the displacement field of each grain, which indicates that different parts of the grain experience different displacement values (Figs 14(c), 14(f), 14(i) and 14(l)).

Two parameters are proposed here for the kinematics analysis: the inertia tensor and the active coordination number. The inertia tensor of each individual grain is a measure of the imbalance in the mass distribution within the grain, which is directly related to grain shape. This tensor is particularly useful for irregular-shaped grains and can be used to quantify the grain resistance to rotation (Wang *et al.*, 2007). The principal moments of inertia (equation (8) in the Appendix) are the eigenvalues of the inertia tensor and the corresponding eigenvectors give the direction of the principal axes. The major eigenvalue is termed I_1, the intermediate I_2 and the minor I_3. The moment of inertia of the grain will be smaller along the longest axis of the grain, which direction

Offprint provided courtesy of www.icevirtuallibrary.com
Author copy for personal use, not for distribution

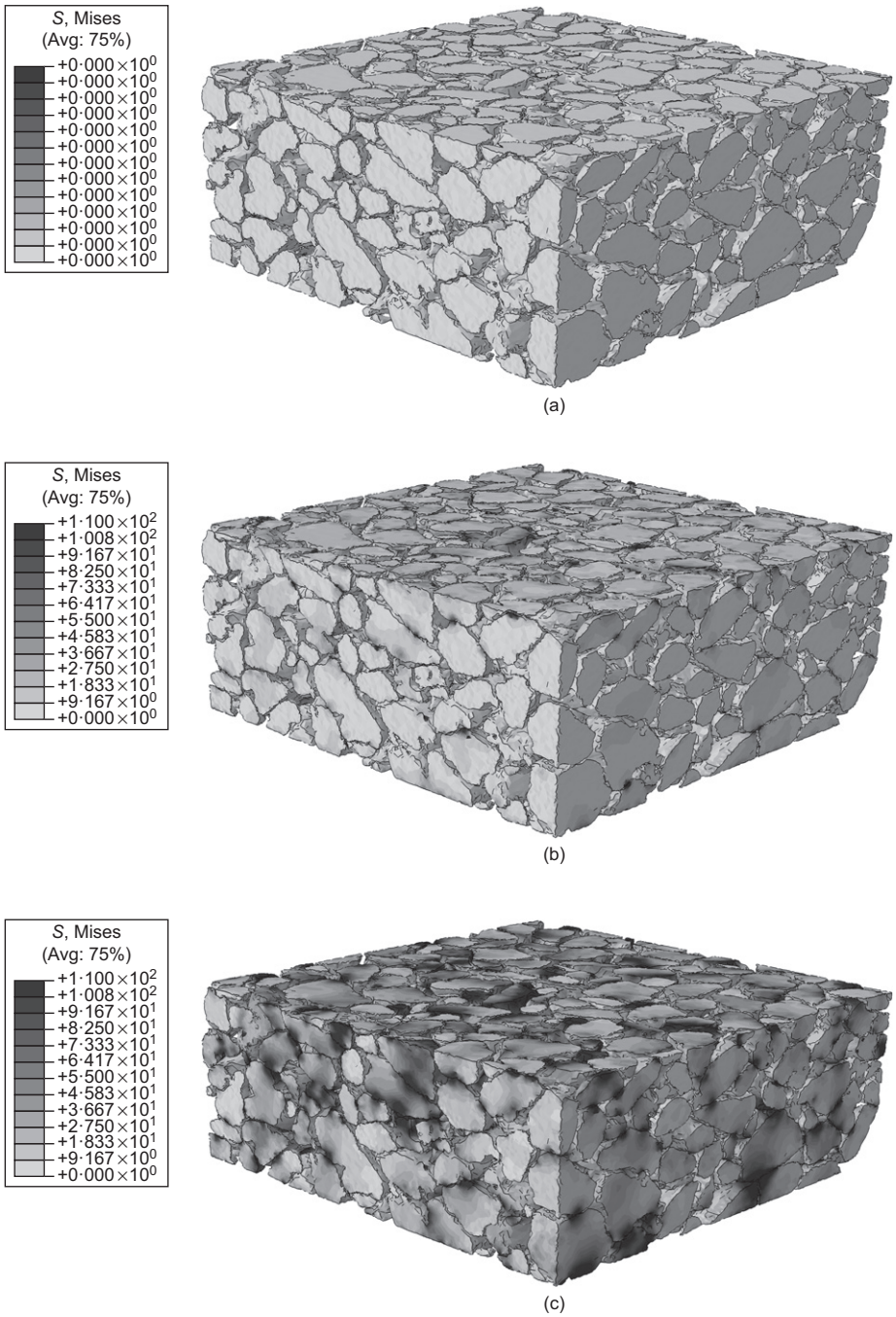

Fig. 13. Granular stress field obtained from the oedometer compression test for the stages: (a) initial ($t = 0$); (b) intermediate ($t = 500$); (c) final ($t = 1000$)

is given by the eigenvector of I_3. This means that the grain is more likely to rotate along this direction. The difference between the magnitude of the three eigenvalues is an indicator of the deviation of the grain shape from a spherical shape ($I_1 = I_2 = I_3$ in the case of a sphere). In Table 1 the inertia tensors and the associated eigenvalues and eigenvectors are presented for the four grains previously discussed. In addition, displacement arrows are used to describe the displacement field in each grain, the magnitude is given by the arrow's size and the direction is given by the vector's direction.

Although the moment of inertia can be directly related to rotational kinematics, in the case of grains belonging to a confined assembly, the resistance to rearrangement is also controlled by the resistance imposed by contacts transmitting stress, the active contacts. In order to better understand the mechanisms that control grain rearrangement within the assembly, grain displacement is related to the inertia tensor and to the number of active contacts (N_{cA}). Referring again to Table 1, it can be seen that the kinematic mechanism tends to become more complex for grains with a larger number of active contacts – for example, 'grain 3' and 'grain 4' when compared with the pure translation observed in 'grain 1' with only one contact.

While in previous figures the authors have presented measurements taken at the final stage of deformation, Fig. 15 demonstrates the ability of this model to measure truly 4D kinematics (the fourth dimension being deformation). Two different grains are presented to show the evolution of the stress and displacement values measured at

Offprint provided courtesy of www.icevirtuallibrary.com
Author copy for personal use, not for distribution

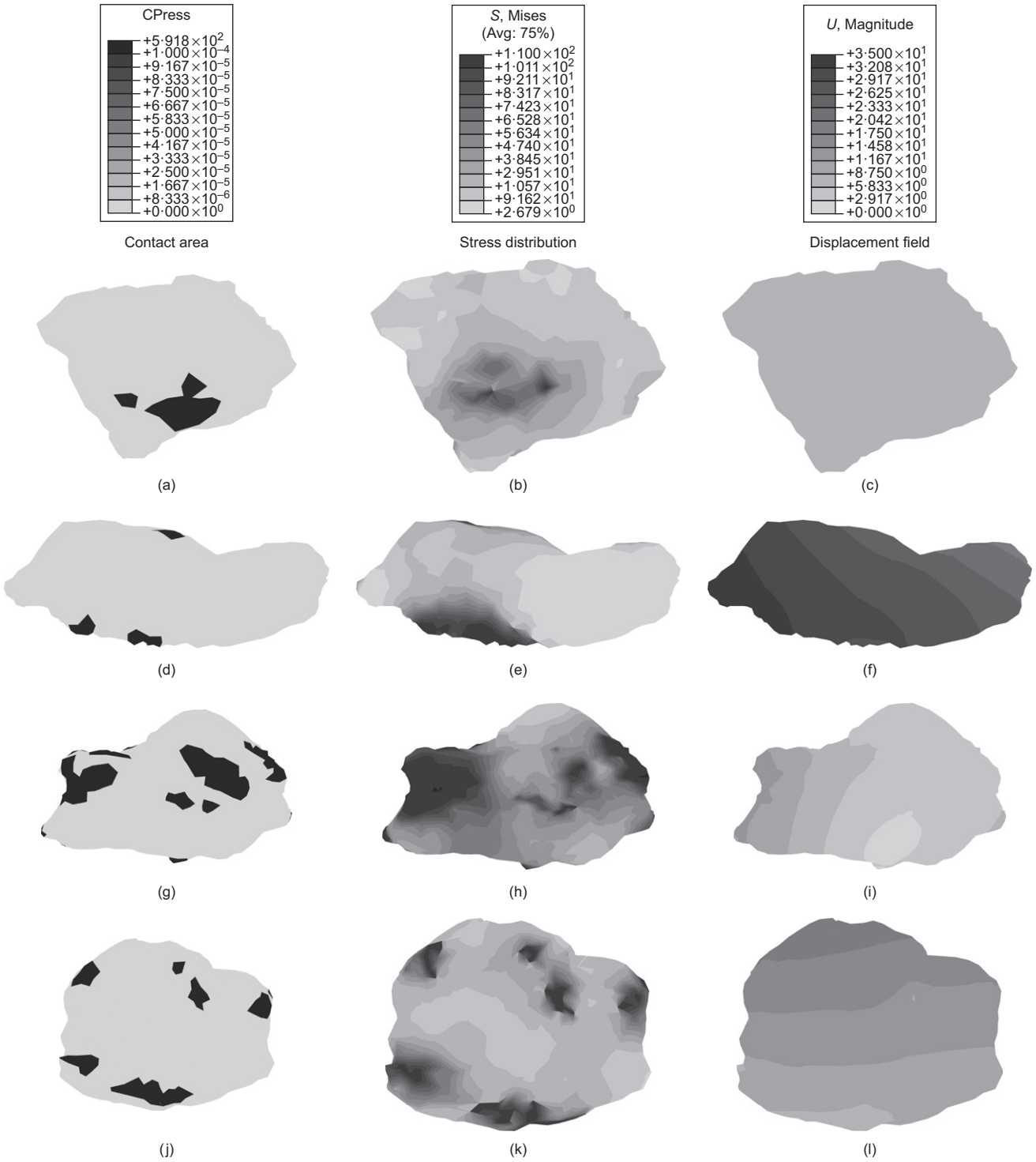

Fig. 14. (a), (d), (g) and (j) Detailed views of the contact areas; (b), (e), (h) and (k) the internal stress distribution; and (c), (f), (i) and (l) displacement field for single grains selected from the assembly, measured at $t = 1000$

a pre-selected point throughout deformation from $t = 0$ to $t = 1000$. For the grain shown in Fig. 15(a) it can be seen that, for t values between 400 and 600, while the displacement increases from 0 to approximately 13 μm the stress values are seen to remain relatively unchanged. Moreover, while for t greater than 600 the displacement remains relatively constant, the stress is seen to undergo a steady increase, suggesting the formation of a highly stressed and stable contact. Further insightful observations on the mechanisms of stress transmission can also be obtained from Fig. 15(b). In this case, as the stress value remains very low and near zero for t values up to 800, it is expected that significant rearrangement occurs during this period. For t greater than 800 the increase in the stress value is accompanied by a significant drop in the increasing rate of displacement and an expected reduction in the rearrangement of this grain.

CONCLUSIONS

The numerical framework presented has an interesting potential to answer long-standing questions on the macro response of soil triggered at the grain level. A key contribution

Offprint provided courtesy of www.icevirtuallibrary.com
Author copy for personal use, not for distribution

Table 1. Analysis of four selected grains in terms of displacement arrows, inertia tensor and the associate eigenvalues and eigenvectors and number of active contacts

ID	Displacement arrows	Inertia tensor	Eigenvalues	Eigenvectors	N_{cA}
1	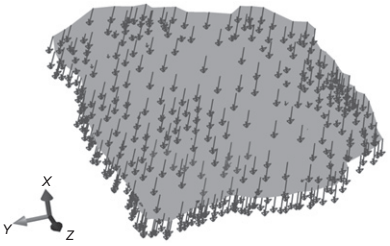	$\begin{bmatrix} 2{\cdot}964 & -3{\cdot}942 & -1{\cdot}649 \\ \cdot & 3{\cdot}401 & -2{\cdot}130 \\ \cdot & \cdot & 5{\cdot}428 \end{bmatrix}$	$I_1 = 7{\cdot}304$ $I_2 = 6{\cdot}245$ $I_3 = -1{\cdot}754$	$\begin{bmatrix} -0{\cdot}538 \\ 0{\cdot}751 \\ -0{\cdot}380 \end{bmatrix}$ $\begin{bmatrix} -0{\cdot}511 \\ 0{\cdot}067 \\ 0{\cdot}856 \end{bmatrix}$ $\begin{bmatrix} 0{\cdot}669 \\ 0{\cdot}655 \\ 0{\cdot}348 \end{bmatrix}$	4
2	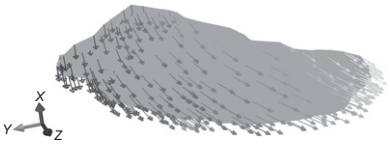	$\begin{bmatrix} 8{\cdot}309 & -1{\cdot}038 & -5{\cdot}157 \\ \cdot & 5{\cdot}625 & 2{\cdot}457 \\ \cdot & \cdot & 3{\cdot}422 \end{bmatrix}$	$I_1 = 12{\cdot}311$ $I_2 = 5{\cdot}308$ $I_3 = -0{\cdot}262$	$\begin{bmatrix} 0{\cdot}778 \\ -0{\cdot}319 \\ -0{\cdot}540 \end{bmatrix}$ $\begin{bmatrix} -0{\cdot}412 \\ -0{\cdot}909 \\ -0{\cdot}056 \end{bmatrix}$ $\begin{bmatrix} 0{\cdot}472 \\ -0{\cdot}267 \\ 0{\cdot}839 \end{bmatrix}$	4
3		$\begin{bmatrix} 4{\cdot}926 & 1{\cdot}124 & 1{\cdot}526 \\ \cdot & 8{\cdot}213 & 8{\cdot}668 \\ \cdot & \cdot & 8{\cdot}005 \end{bmatrix}$	$I_1 = 17{\cdot}067$ $I_2 = 4{\cdot}653$ $I_3 = -0{\cdot}576$	$\begin{bmatrix} 0{\cdot}152 \\ 0{\cdot}701 \\ 0{\cdot}696 \end{bmatrix}$ $\begin{bmatrix} 0{\cdot}986 \\ -0{\cdot}147 \\ -0{\cdot}067 \end{bmatrix}$ $\begin{bmatrix} 0{\cdot}055 \\ 0{\cdot}697 \\ -0{\cdot}714 \end{bmatrix}$	16
4	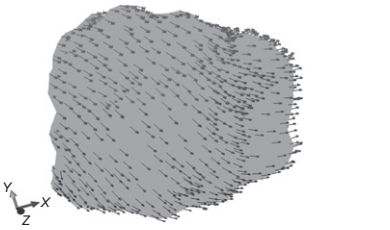	$\begin{bmatrix} 4{\cdot}269 & 3{\cdot}648 & 8{\cdot}891 \\ \cdot & 4{\cdot}519 & 1{\cdot}301 \\ \cdot & \cdot & 4{\cdot}803 \end{bmatrix}$	$I_1 = 14{\cdot}642$ $I_2 = 3{\cdot}651$ $I_3 = -4{\cdot}701$	$\begin{bmatrix} 0{\cdot}678 \\ 0{\cdot}329 \\ 0{\cdot}656 \end{bmatrix}$ $\begin{bmatrix} 0{\cdot}086 \\ -0{\cdot}923 \\ 0{\cdot}373 \end{bmatrix}$ $\begin{bmatrix} 0{\cdot}729 \\ -0{\cdot}196 \\ -0{\cdot}655 \end{bmatrix}$	11

of this method is to enable the stress transmission mechanisms under various load conditions to be inferred. To the best of the present authors' knowledge, the map of internal stresses for real grain morphologies and extended contact surfaces has not been captured previously by any model or experimental analysis. The results presented here demonstrate that heterogeneous force transfer networks can be characterised while accounting for the effect of contact topology, grain morphology and the preferential orientation of the grains. The displacement field obtained for each individual grain allows an accurate characterisation of the grain kinematics based on a truly 4D quantification of fabric evolution throughout deformation. By combining an inertia tensor with the distribution of the active contact areas it is possible to gain an improved understanding of grain kinematics under loading. Although computationally expensive, the model is instrumental for clarifying the fundamentals of granular media at the grain scale that need to be considered when modelling their mechanical behaviour. Future work will include the refinement of this simulation technique through direct comparison with experiments and expansion of the model to include grain breakage. Finally, the μFE model presented here can offer significant insight into the micro phenomena triggered by the rich topologies found in natural soil, which have been insufficiently represented in traditional numerical simulation approaches.

APPENDIX

Delaunay refined algorithm

The efficiency and robustness of Delaunay triangulation makes it the most commonly used unstructured triangulation algorithm (Chen & Xu, 2004). In order to optimise the triangulation, the Delaunay approach gives a set of 'quality' triangles to use as polygons presenting the extracted surface (Shewchuk, 2014). The challenge is to find a triangulation that covers the surface of individual objects, in this case the grains, while satisfying shapes and size constraints (the angles should not be too small or too large; similarly, the triangles should not be very small or very large). For ease of visualisation, a 2D example is presented here to illustrate the refinement process (Fig. 16). For this particular case, the input data are a polygonal region with constraining edges and vertices inside the region. The aim is to generate a

Offprint provided courtesy of www.icevirtuallibrary.com
Author copy for personal use, not for distribution

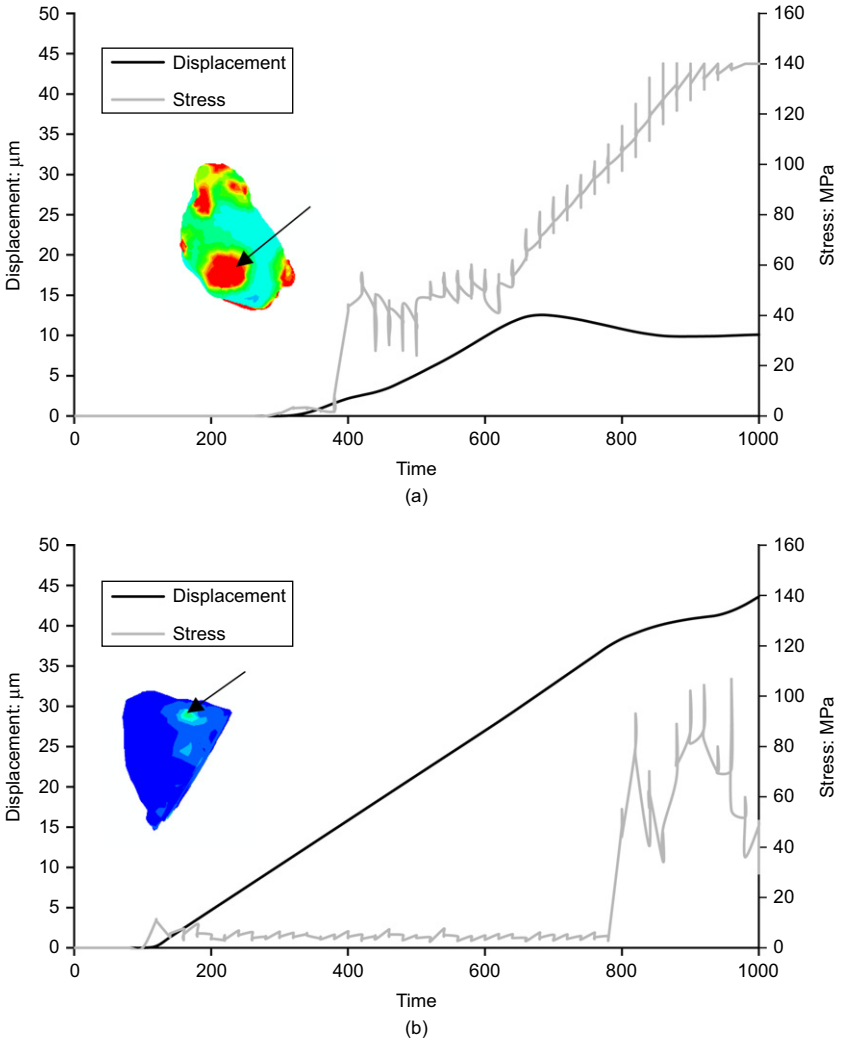

Fig. 15. Evolution of point stress and displacement values measured at two selected grains throughout deformation from $t = 0$ to $t = 1000$

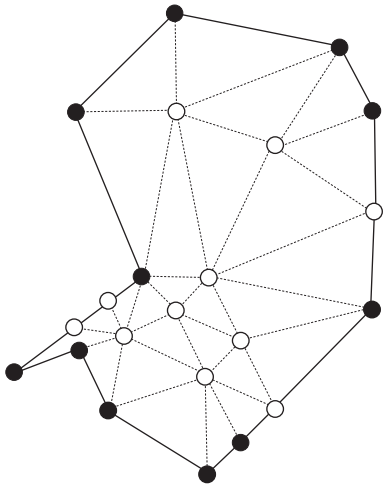

Fig. 16. Example of a 2D triangulation problem, the input data are represented by the solid vertices and edges and the obtained triangulation is given by the hollow vertices and dashed edges

triangulation of the region whose edges and vertices cover all input edges and vertices. A triangulation of the input is obtained by taking a subset of triangles. As shown in Fig. 16, the input data are represented by solid vertices and edges and the output for this meshing problem is represented by hollow vertices and dashed edges. The quality of triangles, in terms of size and shape, is commonly controlled by assessing the smallest and largest internal angles and the aspect ratio. Here, the threshold approach is used to generate an output such that its smallest angle is not less than some predefined threshold (Shewchuk, 2002). A practical way to deal with sharp input features is to isolate them during the refining process so they do not reduce the quality of the triangulation. The triangulation output is refined by adding more points to resolve triangles with very small and/or very large angles and cover edges that may not covered. In general, Delaunay algorithms consist of maintaining a constrained Delaunay triangulation, which is refined by inserting carefully placed vertices until the mesh meets the constraints on triangle quality and size.

Inertia tensor

The inertia tensor is defined as follows

$$\boldsymbol{I} = \begin{bmatrix} I_{xx} & I_{xy} & I_{xz} \\ I_{xx} & I_{yy} & I_{yz} \\ I_{zx} & I_{zy} & I_{zz} \end{bmatrix} = \begin{bmatrix} \int (y^2 + z^2)\mathrm{d}m & -\int xy\mathrm{d}m & -\int xz\mathrm{d}m \\ -\int xy\mathrm{d}m & \int (x^2 + z^2)\mathrm{d}m & -\int yz\mathrm{d}m \\ -\int zx\mathrm{d}m & -\int zy\mathrm{d}m & \int (x^2 + y^2)\mathrm{d}m \end{bmatrix} \tag{8}$$

where the quantities I_{xx}, I_{yy}, and I_{zz} are termed moments of inertia and the quantities I_{xy}, I_{xz}, I_{yx}, I_{yz}, I_{zx} and I_{zy} are the products of inertia.

Offprint provided courtesy of www.icevirtuallibrary.com
Author copy for personal use, not for distribution

ACKNOWLEDGEMENTS

The authors would like to thank City, University of London for the doctoral scholarship of the first author. This paper uses image data from the doctoral research of the second author, for which the contributions of Dr Catherine O'Sullivan from Imperial College London and Professor Matthew Coop from University College London are gratefully acknowledged.

NOTATION

a	radius of contact area
D	depth
D_e	watershed depth
D_{max}	maximum depth of all catchment basins
d_{50}	median grain diameter
E	elastic modulus
E_K	kinetic energy
E_t	hardening modulus
E_U	internal energy
$\dot{E}_{WF}$	external work
$\boldsymbol{F}$	applied load vector
$\boldsymbol{F}_c$	contact forces vector
$\boldsymbol{F}_{ext}$	applied external loads vector
$\boldsymbol{F}_i$	internal force vector
$\boldsymbol{F}_{int}$	internal resisting forces vector
F_n	normal contact force
F_t	tangential contact force
G	shear modulus
h	overclosure
I_{xx}	moments of inertia around x axis
I_{xy}, I_{yx}	products of inertia on xy plane
I_{xz}, I_{zx}	products of inertia on xz plane
I_{yy}	moments of inertia around y axis
I_{yz}, I_{zy}	products of inertia on yz plane
I_{zz}	moments of inertia around z axis
K	bulk modulus
l	level parameter
$\mathbf{M}$	mass matrix
M_T	twisting moment
m	mass
N_{cA}	number of active contacts
p	pressure
Q_x	traction force in x direction
R	radius
T	threshold parameter
t	time
U	internal energy per unit mass
u	displacement
$\dot{u}$	velocity
$\ddot{u}$	acceleration
V	volume
$\boldsymbol{v}$	velocity field vector
$\boldsymbol{x}$	nodal displacement vector
β	twisting angle
ε_x	Johnson's creep model
μ	friction coefficient
Π	virtual work
ρ	density
σ_y	yield stress

REFERENCES

Alonso-Marroquin, F., Luding, S., Herrmann, H. J. & Vardoulakis, I. (2005). Role of anisotropy in the elastoplastic response of a polygonal packing. *Phys. Rev. E* **71**, No. 5, 051304-(1–18).

Andrade, J. E., Lim, K. W., Avila, C. F. & Vlahinić, I. (2012). Granular element method for computational particle mechanics. *Comput. Methods Appl. Mech. Engng* **241–244**, 262–274, https://doi.org/10.1016/j.cma.2012.06.012.

Atwood, R. C., Jones, J. R., Lee, P. D. & Hench, L. L. (2004) Analysis of pore interconnectivity in bioactive glass foams using X-ray microtomography. *Scripta Materialia* **51**, No. 11, 1029–1033.

Azéma, E. & Radjai, F. (2012). Force chains and contact network topology in sheared packings of elongated particles. *Phys. Rev. E* **85**, No. 3, 031303.

Beucher, S. & Lantuejoul, C. (1979). *Use of watersheds in contour detection*. Rennes, France: CCETT.

Brunke, O., Brockdorf, S., Drews, K., Muller, B., Donath, T., Herzen, J. and Felix Beckmann, F. (2008). Comparison between X-ray tube based and synchrotron radiation based microCT. In *Developments in X-ray tomography VI* (ed. S. R. Stock), Proceedings of SPIE volume 7078, paper 70780U. Bellingham, WA, USA: SPIE.

Cavarretta, I. & O'Sullivan, C. (2012). The mechanics of rigid irregular particles subject to uniaxial compression. *Géotechnique* **62**, No. 8, 681–692, http://dx.doi.org/10.1680/geot.10.P.102.

Cavarretta, I., Coop, M. & O'Sullivan, C. (2010). The influence of particle characteristics on the behaviour of coarse grained soils. *Géotechnique* **60**, No. 6, 413–423, http://dx.doi.org/10.1680/geot.2010.60.6.413.

Chen, L. & Xu, J. (2004). Optimal Delaunay triangulations. *J. Comput. Math.* **22**, No. 2, 299–308.

Cil, M. B. & Alshibli, K. A. (2014). 3D evolution of sand fracture under 1D compression. *Géotechnique* **64**, No. 5, 351, http://dx.doi.org/10.1680/geot.13.P.119.

Cole, D. M., Mathisen, L. U., Hopkinks, M. A. & Knapp, B. R. (2010). Normal and sliding contact experiments on gneiss. *Granular Matter* **12**, No. 1, 69–86.

Cundall, P. A. & Strack, O. D. L. (1979). A discrete numerical model for granular assemblies. *Géotechnique* **29**, No. 1, 47–65, http://dx.doi.org/10.1680/geot.1979.29.1.47.

Dassault Systèmes (2014). *ABAQUS user's manual 2014* version 6.14. Providence, RI, USA: Dassault Systèmes.

Druckrey, A. M., Alshibli, K. A. & Al-Raoush, R. I. (2016). 3D characterization of sand particle-to-particle contact and morphology. *Comput. Geotech.* **74**, 26–35, https://doi.org/10.1016/j.compgeo.2015.12.014.

Ferellec, J. F. & McDowell, G. R. (2010). A method to model realistic particle shape and inertia in DEM. *Granular Matter* **12**, No. 5, 459–467.

Fonseca, J. (2011). *The evolution of morphology and fabric of a sand during shearing*. PhD thesis, Imperial College London, University of London, London, UK.

Fonseca, J., O'Sullivan, C., Coop, M. R. & Lee, P. D. (2012). Non-invasive characterization of particle morphology of natural sands. *Soils Found.* **52**, No. 4, 712–722.

Fonseca, J., O'Sullivan, C., Coop, M. R. & Lee, P. D. (2013a). Quantifying the evolution of soil fabric during shearing using scalar parameters. *Géotechnique* **63**, No. 10, 818–829, http://dx.doi.org/10.1680/geot.11.P.150.

Fonseca, J., O'Sullivan, C., Coop, M. R. & Lee, P. D. (2013b). Quantifying the evolution of soil fabric during shearing using directional parameters. *Géotechnique* **63**, No. 6, 487–499, http://dx.doi.org/10.1680/geot.12.P.003.

Fonseca, J., Bésuelle, P. & Viggiani, G. (2013c). Micromechanisms of inelastic deformation in sandstones: an insight using x-ray micro-tomography. *Géotechnique Lett.* **3**, No. 2, 78–83, http://dx.doi.org/10.1680/geolett.13.034.

Fonseca, J., Nadimi, S., Reyes-Aldasoro, C. C., O'Sullivan, C. & Coop, M. R. (2016). Image-based investigation into the primary fabric of stress transmitting particles in sand. *Soils Found.* **56**, No. 5, 818–834.

Harthong, B., Jérier, J., Richefeua, V., Chareyre, B., Dorémus, P., Imbault, D. & Donzé, F. (2012). Contact impingement in packings of elastic–plastic spheres, application to powder compaction. *Int. J. Mech. Sci.* **61**, No. 1, 32–43.

Hertz, H. (1882). Über die Berührung fester elastischer Körper. *J. für die reine und angewandte Mathematik* **92**, 156–171 (in German).

Holtzman, R., Silin, D. B. & Patzek, T. W. (2009). Mechanical properties of granular materials: a variational approach to grain-scale simulations. *Int. J. Numer. Analyt. Methods Geomech.* **33**, No. 3, 391–404.

Ibanez, L., Schroeder, W., Ng, L. & Cates, J. (2005). *The ITK software guide*. Clifton Park, NY, USA: Kitware Inc.

Katagiri, J., Matsushima, T. & Yamada, Y. (2010). Simple shear simulation of 3D irregularly-shaped particles by image-based DEM. *Granular Matter* **12**, No. 5, 491–497.

Offprint provided courtesy of www.icevirtuallibrary.com
Author copy for personal use, not for distribution

Katagiri, J., Matsushima, T., Yamada, Y., Tsuchiyama, A., Nakano, T., Uesugi, K., Ohtake, M. & Saiki, K. (2014). Investigation of 3D grain shape characteristics of lunar soil retrieved in Apollo 16 using image based discrete element modeling. *J. Aerospace Engng, ASCE* **28**, No. 4, 04014092.

Kawamoto, R., Andò, E., Viggiani, G. & Andrade, J. E. (2016). Level set discrete element method for three-dimensional computations with triaxial case study. *J. Mech. Phys. Solids* **91**, 1–13, https://doi.org/10.1016/j.jmps.2016.02.021.

Lorensen, W. & Cline, H. (1987). Marching cubes: a high resolution 3D surface construction algorithm. Computer Graphics. In *Proceedings of 14th annual conference on computer graphics and interactive techniques, siggraph '87* (ed. M. C. Stone), pp. 163–169. New York, NY, USA: Association for Computing Machinery (ACM).

Lu, M. & McDowell, G. R. (2007). The importance of modelling ballast particle shape in the discrete element method. *Granular Matter* **9**, No. 1, 69–80.

Luding, S. & Bauer, E. (2011). Evolution of swelling pressure of cohesive–frictional, rough and elasto-plastic granulates. In *Geomechanics and geotechnics: from micro to macro (IS-Shanghai conference proceedings)* (eds M. J. Jiang, F. Liu and M. Bolton), pp. 495–499. Rotterdam, the Netherlands: CRC Press/Balkema.

Mathworks (2015). *MATLAB release R2015b*. Natick, MA, USA: Mathworks, Inc.

Matsushima, T. & Chang, C. S. (2011). Quantitative evaluation of the effect of irregularly shaped particles in sheared granular assemblies. *Granular Matter* **13**, No. 3, 269–276.

Matsushima, T., Katagiri, J., Uesugi, K., Tsuchiyama, A. & Nakano, T. (2009). 3D shape characterization and image-based DEM simulation of the lunar soil simulant FJS-1. *J. Aerospace Engng* **22**, No. 1, 15–23.

Mindlin, R. D. & Deresiewiez, H. (1953). Elastic spheres in contact under varying oblique forces. *ASME J. Appl. Mech.* **20**, 327–344.

Miskin, M. Z. & Jaeger, H. M. (2013). Adapting granular materials through artificial evolution. *Nature Mater.* **12**, No. 4, 326–331.

Munjiza, A. (2004). *The combined finite-discrete element method*. Chichester, UK: John Wiley & Sons.

Nadimi, S. & Fonseca, J. (2017). On the tensile strength of soil grains in Hertzian response. In *Powders and grains 2017 – 8th international conference on micromechanics on granular media* (eds F. Radjai, S. Nezamabadi, S. Luding and J. Y. Delenne), EPJ Web of Conferences Vol. 140, paper 07001. Les Ulis, France: EDP Sciences – Web of Conferences.

Nadimi, S., Fonseca, J. & Taylor, R. N. (2015). A microstructure-based finite element analysis of the response of sand. In *Deformation characteristics of geomaterials* (eds V. A. Rinaldi, M. E. Zeballos and J. J. Clariá), pp. 816–823. Amsterdam, the Netherlands: IOS Press.

Nguyen, D., Azéma, E., Sornay, P. & Radjai, F. (2015). Effects of shape and size polydispersity on strength properties of granular materials. *Phys. Rev. E* **91**, No. 3, 032203.

Oda, M. & Iwashita, K. (1999). *Mechanics of granular materials, an introduction*. Rotterdam, the Netherlands: CRC Press.

Otsu, N. (1979). A threshold selection method from gray-level histograms. *IEEE Trans. Systems, Man and Cybernetics* **9**, No. 1, 62–66.

Pasha, M., Dogbe, S., Hare, C., Hassanpour, A. & Ghadiri, M. (2014). A new linear contact model for elasto-plastic and adhesive contacts in Distinct Element Method. *Granular Matter* **16**, No. 1, 151–162.

Radjai, F. (2008). Particle-scale origins of shear strength in granular media. *Second Euro-Mediterranean symposium on advances in geomaterials and structures (AGS08)*, Hammamet, Tunisia.

Rineau, L. & Yvinec, M. (2017). 3D surface mesh generation. In *CGAL user and reference manual*, 4.10 edn, chapter 53. Valbonne, France: CGAL Editorial Board, Geometry Factory.

Schindelin, J., Rueden, C. T., Hiner M. C. & Eliceiri K. W. (2015) The ImageJ ecosystem: an open platform for biomedical image analysis. *Molecular Reproduction and Development* **82**, No. 7–8, 518–529.

Senetakis, K., Coop, M. R. & Todisco, M. C. (2013). The inter-particle coefficient of friction at the contacts of Leighton Buzzard sand quartz minerals. *Soils Found.* **53**, No. 5, 746–755.

Shewchuk, J. R. (2002). Constrained Delaunay tetrahedralizations and probably good boundary recovery. *Proceedings of the 11th international meshing roundtable*, Ithaca, NY, USA, pp. 193–204.

Shewchuk, J. R. (2014). Reprint of: Delaunay refinement algorithms for triangular mesh generation. *Computational Geometry: Theory and Applications* **47**, No. 7, 741–778.

Thakur, S. C., Morrissey, J. P., Sun, J., Chen, J. F. & Ooi, J. Y. (2014). Micromechanical analysis of cohesive granular materials using the discrete element method with an adhesive elasto-plastic contact model. *Granular Matter* **16**, No. 3, 383–400.

Wang, L., Park, J. Y. & Fu, Y. (2007). Representation of real particles for DEM simulation using X-ray tomography. *Constr. Building Mater.* **21**, No. 2, 338–346.

Wu, S. R. (2006). Lumped mass matrix in explicit finite element method for transient dynamics of elasticity. *Comput. Methods Appl. Mech. Engng.* **195**, No. 44–47, 5983–5994.

Yang, Y., Wang, J. F. & Cheng, Y. M. (2016). Quantified evaluation of particle shape effects from micro-to-macro scales for non-convex grains. *Particuology* **25**, 23–35.

Zheng, Q. J., Zhu, H. P. & Yu, A. B. (2012). Finite element analysis of the contact forces between a viscoelastic sphere and rigid plane. *Powder Technol.* **226**, 130–142.

Zhou, B. & Wang, J. (2017). Generation of a realistic 3D sand assembly using X-ray micro-computed tomography and spherical harmonic-based principal component analysis. *Int. J. Numer. Analyt. Methods Geomech.* **41**, 93–109, http://dx.doi.org/10.1002/nag.2548.

Offprint provided courtesy of www.icevirtuallibrary.com
Author copy for personal use, not for distribution